ROYAL SOCIETY
OF CHEMISTRY

PAPER

Check for updates

Cr$_2$TiC$_2$T$_x$ MXene as an adsorbent material in ultrasonic-assisted d-μ-solid phase extraction for trace detection of heavy metals†

Saman Bagheri, [ID] * Rashmeet Kaur Khurana, Md. Ibrahim Kholil, [ID]
Michael J. Loes, [ID] Shengyuan Luo [ID] and Alexander Sinitskii [ID] *

MXenes are a large family of two-dimensional transition metal carbides, nitrides, and carbonitrides. While MXenes have great potential for applications in analytical chemistry, most of the studies in this field are focused on Ti$_3$C$_2$T$_x$, the most popular MXene material. For example, several studies employed Ti$_3$C$_2$T$_x$ as an adsorbent for the trace detection of toxic analytes, but there is limited knowledge on the utility of other MXene materials for this application. In this work, we investigated the potential of Cr$_2$TiC$_2$T$_x$, one of the least studied MXenes, for application as an adsorbent material in ultrasonic-assisted dispersive micro solid-phase extraction (d-μ-SPE) method for the detection of heavy metals at trace levels in food and soil samples. We synthesized large monolayer flakes of Cr$_2$TiC$_2$T$_x$ and characterized it by a variety of microscopic and spectroscopic techniques. Cr$_2$TiC$_2$T$_x$ MXene showed remarkable performance in the d-μ-SPE method with the detection limits of 0.09 and 1.9 ng mL^{-1}, and dynamic ranges of 0.3–90 μg L^{-1} and 6–120 μg L^{-1} for cadmium (Cd^{2+}) and lead (Pb^{2+}) ions, respectively. The great performance of Cr$_2$TiC$_2$T$_x$ MXene as an adsorbent for the trace detection of heavy metals highlights the importance of investigating other MXenes beyond Ti$_3$C$_2$T$_x$ for analytical applications.

1. Introduction

MXenes are an emerging family of two-dimensional materials with a general formula of M$_{n+1}$X$_n$T$_x$, where M is a transition metal, such as Ti, Mo, V, *etc.*, X is carbon and/or nitrogen, *n* = 1, 2, 3, 4, or 5, and T$_x$ represents the surface functional groups.[1–3] Since their discovery in 2011,[4] MXenes have grown into a large field of research.[1–3] Significant effort in this field has been dedicated to developing new MXene materials by experimenting with various combinations of M and X elements. This effort has experimentally advanced over 40 different MXenes.[1–3] However, research on MXene applications has been predominantly focused on Ti$_3$C$_2$T$_x$, the most studied MXene to date.[1–3] The general preference for Ti$_3$C$_2$T$_x$ stems from its straightforward synthesis, which has been thoroughly optimized over the last decade to yield large monolayer flakes of high quality.[5–7]

One of the MXene materials that received less attention than Ti$_3$C$_2$T$_x$ is Cr$_2$TiC$_2$T$_x$. It is synthesized by etching

Department of Chemistry and Nebraska Center for Materials and Nanoscience, University of Nebraska-Lincoln, Lincoln, Nebraska 68588, USA.
E-mail: sbagheri2@unl.edu, sinitskii@unl.edu

† Electronic supplementary information (ESI) available. See DOI: https://doi.org/10.1039/d4nr02556c

Cr$_2$TiAlC$_2$, a layered quaternary MAX phase, where a Ti layer is sandwiched between two Cr–C layers (⋯Cr–C–Ti–C–Cr–Al⋯). While the transition metals mostly occupy different layers, a recent study demonstrated that a certain number of Cr atoms may also be present in the Ti layer.[8] The first detailed study on the synthesis and physical properties of Cr$_2$TiC$_2$T$_x$ was reported by Hantanasirisakul and co-workers.[9] In that study, the authors etched Cr$_2$TiAlC$_2$ and exfoliated it into Cr$_2$TiC$_2$T$_x$ using a mixture of HF/HCl as the etchant and TMAOH as the intercalating agent. For delamination, the sample was sonicated and a solution of monolayer MXene flakes with lateral sizes in sub-μm range was collected. Building upon this foundational work, we optimized the synthesis process and produced Cr$_2$TiC$_2$T$_x$ flakes with larger sizes in μm range, with minimal degradation and defects.

Trace detection of contaminating agents and toxins using MXenes is still a relatively uncharted territory. The studies reported so far overwhelmingly utilized Ti$_3$C$_2$T$_x$[10–17] and explored applications such as electrochemical sensors, purification, and extraction.[18–22] Considering the pool of published literature, there remains a significant gap in the exploration and understanding of other MXene materials, such as Cr$_2$TiC$_2$T$_x$, for which there is no case study on their performance in trace detection of heavy metals. In this work, we investigated the potential of Cr$_2$TiC$_2$T$_x$ MXene as an adsorbent in
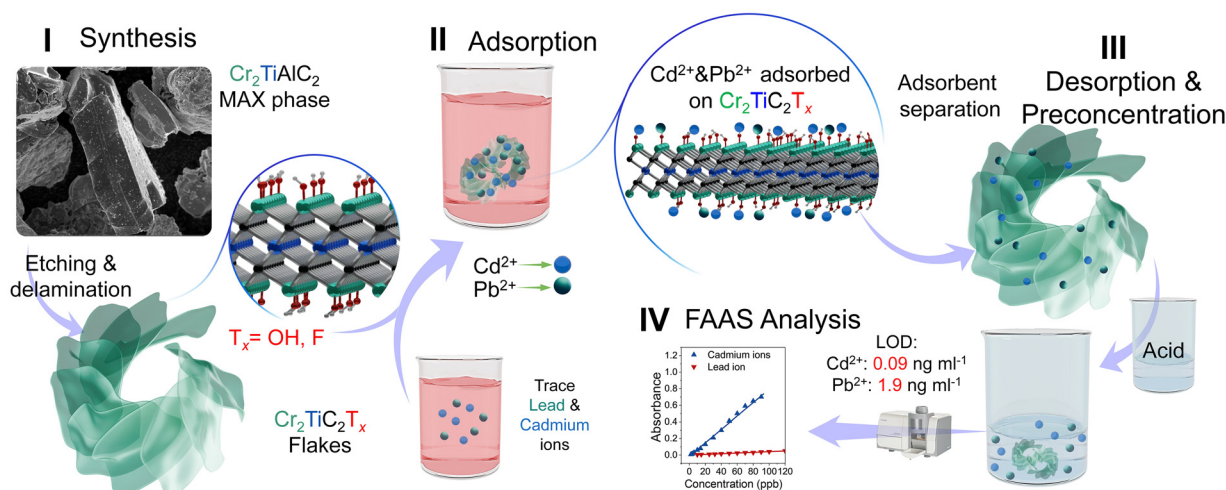
Scheme 1 Schematic illustration of the application of $Cr_2TiC_2T_x$ MXene as a solid phase in ultrasonic-assisted d-μ-SPE for heavy metal detection.

ultrasonic-assisted dispersive micro solid-phase extraction (d-μ-SPE) for the trace detection of heavy metal ions, Cd^{2+} and Pb^{2+}.

The structure of this work is demonstrated in Scheme 1, which shows that we first synthesized $Cr_2TiC_2T_x$ (I), and then utilized it for the adsorption of Cd^{2+} and Pb^{2+} ions (II) that were present in trace amounts in analytical samples. After the extraction of the MXene material, the heavy metal ions were desorbed from $Cr_2TiC_2T_x$ flakes using an acid (III), which resulted in preconcentrated samples that were suitable for analysis by flame atomic absorption spectrometry (FAAS, IV). After the desorption of Cd^{2+} and Pb^{2+} ions, the MXene material can be reused for preconcentration of heavy metal ions from other analytical samples. We studied the adsorption properties, structural stability, and efficiency of $Cr_2TiC_2T_x$ in detecting trace concentrations of Cd^{2+} and Pb^{2+} ions. We demonstrate that $Cr_2TiC_2T_x$ exhibits attractive properties as an adsorbent in ultrasonic-assisted d-μ-SPE, offering high sensitivity, stability, and performance.

2. Experimental

2.1. Reagents and materials

Ti (99%, 325 mesh), Al (99%, 325 mesh), and Cr (99.9%, 325 mesh) were purchased from Alfa Aesar. Concentrated hydrochloric acid (HCl), nitric acid (HNO₃), and acetic acid (CH₃COOH) were purchased from Thermo Fisher Scientific. Tetramethylammonium hydroxide (TMAOH, 25 wt% in methanol), hydrofluoric acid (48–52% HF), lead nitrate (Pb(NO₃)₂), and cadmium nitrate tetrahydrate (Cd(NO₃)₂·4H₂O) were purchased from Sigma-Aldrich. Heavy metal stock solutions were prepared by dissolving appropriate amounts of the metal salts in double-distilled water.

2.2. Synthesis

For the Cr_2TiAlC_2 MAX phase synthesis, the elemental precursors, Cr, Ti, Al, and graphite, taken at a ratio of 2 : 1 : 1.2 : 1.9,

were thoroughly mixed using a pestle and mortar, transferred into an alumina crucible, and annealed at 1450 °C under the flow of argon (450 sccm) for 8 h. The prepared MAX phase was crushed and sieved to obtain particles with sizes of 30–40 μm.

For the synthesis of $Cr_2TiC_2T_x$ MXene, 6 g of the MAX phase was slowly added to a solution containing 18 mL of HF, 32 mL of HCl, and 45 mL of H₂O and stirred at 600 rpm with a 2-inch stir bar for 48 h at room temperature (25 °C). The etching product was washed with deionized (DI) water to reach pH 7 before intercalation. Then, 6 mL of TMAOH solution (25 wt% in methanol) was mixed with 24 mL of H₂O and used to intercalate multilayer MXene particles for 24 h at room temperature. After the intercalation, the solution was centrifuged at 10 000 rpm and washed with DI water to pH 7 using a 500 mL round-bottom centrifuge tube. Finally, the $Cr_2TiC_2T_x$ MXene was delaminated in 50 mL of DI water through mild shaking for 20–30 min, centrifuged at 1500 rpm for 5 min, and vacuum dried for further experiments.

2.3. Materials characterization

Concentrations of cadmium and lead ions were analyzed by a 3100 PerkinElmer FAAS spectrometer using an air-acetylene flame. Cadmium (228.8 nm) and lead (283.3 nm) hollow cathode lamps were used as radiation sources. The pH measurements were performed at 25 ± 1 °C using a digital Accumet AB150 ion analyzer supplied with a combined glass-calomel electrode. The morphology of MXene samples was studied by scanning electron microscopy (SEM) using an FEI Nova NanoSEM 450 instrument at the accelerating voltage of 5 kV. Transmission electron microscopy (TEM), scanning transmission electron microscopy (STEM), selected area electron diffraction (SAED), and energy-dispersive X-ray (EDX) spectroscopy were performed using an FEI Tecnai Osiris instrument (200 kV) on MXene flakes deposited on lacey carbon TEM grids.

Brunauer–Emmett–Teller (BET) surface area analysis was performed using a Micrometrics ASAP 2460 surface area and porosimetry analyzer by recording nitrogen adsorption isotherms at −196 °C. Before the adsorption experiments, all samples were dried at 120 °C for 24 h under N_2. The standard BET procedure involving the nitrogen adsorption–desorption data collected at a relative equilibrium pressure interval was used to calculate the specific surface areas of the samples. The amount of nitrogen adsorbed at the relative pressure of 0.985 was used to estimate the total pore volume. X-ray diffraction (XRD) patterns were recorded by a PANalytical Empyrean powder diffractometer with Ni-filtered Cu Kα radiation operated at 40 kV and 30 mA using a step size of 0.03° and 1 s dwelling time. The chemical analysis of the prepared samples was carried out by X-ray photoelectron spectroscopy (XPS) using a Thermo Scientific K-alpha X-ray photoelectron spectrometer with monochromatic Al Kα (1486.6 eV) radiation and a flood gun for charge compensation.

3. Results and discussion

3.1. $Cr_2TiC_2T_x$ synthesis and characterization

After the synthesis, Cr_2TiAlC_2 was crushed into a powder, and a fraction of particles with sizes of 30–40 μm was collected by sieving. The progression of these steps is demonstrated in Fig. 1, where we show an optical image of a sintered Cr_2TiAlC_2 pellet in Fig. 1a, a crushed MAX phase powder in Fig. 1b, and an SEM image of the sieved particles in Fig. 1c.

After collecting powdered Cr_2TiAlC_2 material, the MAX phase was etched in a mixture of HF, HCl, and H_2O for 48 h. Upon completion, the compact MAX phase particles transformed into MXene accordion-like structures[7,23] as aluminum atoms were removed from Cr_2TiAlC_2. An SEM image of representative accordion-like structures with split MXene layers is shown in Fig. 1d. The delamination of accordion-like structures into monolayer $Cr_2TiC_2T_x$ flakes was performed as described in the Experimental section, resulting in an aqueous suspension of MXene sheets. A vacuum filtration of this suspension produced a uniform $Cr_2TiC_2T_x$ film that is shown in the SEM image in Fig. 1e. The film consists of stacked MXene flakes with no signs of MAX phase particles. The TEM analysis in Fig. 1f also confirms the formation of uniform $Cr_2TiC_2T_x$ flakes with lateral sizes of a few μm. The SAED pattern in Fig. 1g demonstrates the hexagonal arrangement of the diffraction spots, corresponding to the structure of $Cr_2TiC_2T_x$. The expected uniform distribution of Ti and Cr elements in $Cr_2TiC_2T_x$ flakes was confirmed by the STEM-EDX analysis in Fig. 1h. Finally, the monolayer character of MXene flakes was
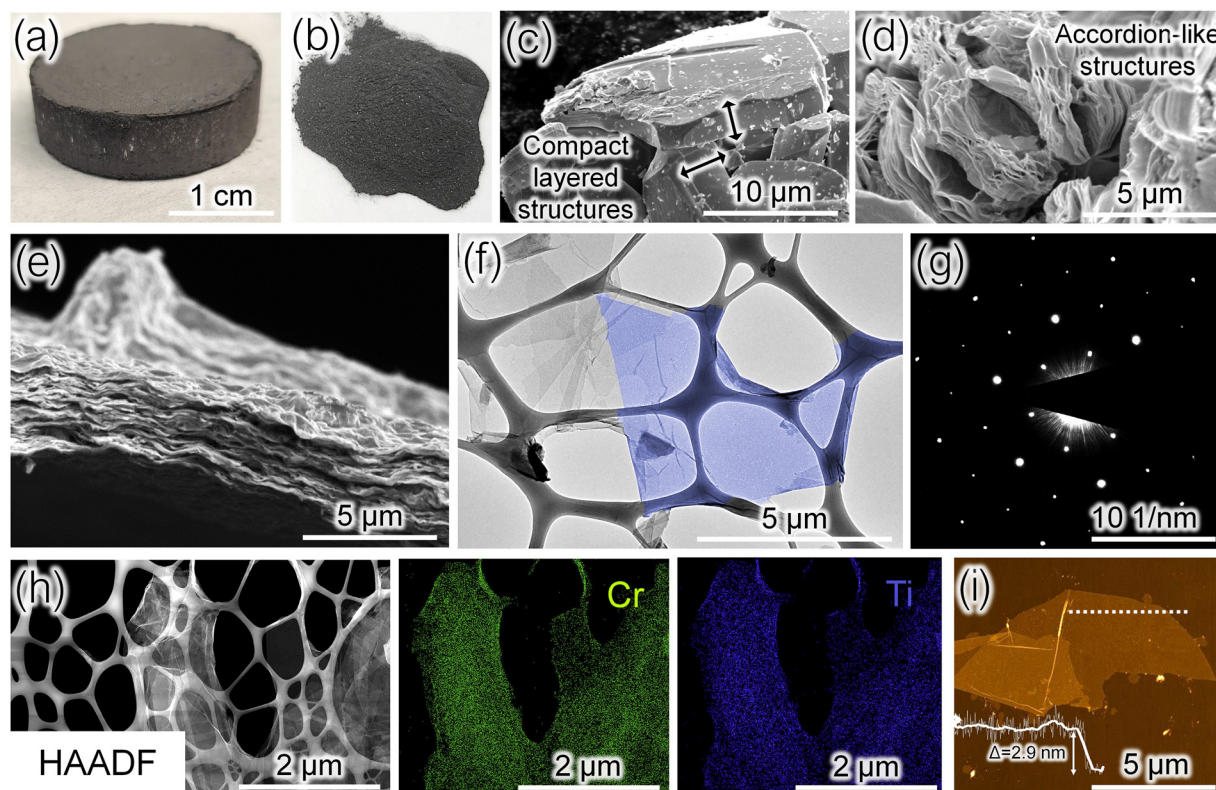

Fig. 1 Microscopy analysis of $Cr_2TiC_2T_x$ MXene. (a) Optical image of a sintered pellet of Cr_2TiAlC_2 MAX phase. (b) Optical image of a powdered sample of Cr_2TiAlC_2 MAX phase. (c) SEM image of Cr_2TiAlC_2 MAX phase crystals. (d) SEM image of accordion-like structure of $Cr_2TiC_2T_x$. (e) SEM image of $Cr_2TiC_2T_x$ film formed by stacked MXene flakes. (f) TEM image of $Cr_2TiC_2T_x$ flakes on a lacey carbon grid. One of the flakes is colored blue for clarity to distinguish it from the weblike structure of the lacey carbon support. (g) SAED pattern of the flake shown in (f) in false color. (h) HAADF image of MXene flakes and their EDX elemental maps for Cr and Ti. (i) AFM image of a monolayer $Cr_2TiC_2T_x$ flake with a thickness of about 2.9 nm. The flake was visualized on a Si/SiO$_2$ substrate; the height profile was measured along the white dotted line.

confirmed by AFM. An AFM image of a monolayer $Cr_2TiC_2T_x$ flake with a lateral size of 10 μm and a thickness of about 2.9 nm is shown in Fig. 1i. Similar thicknesses of about 2.5 nm were previously reported for the monolayer flakes of $Ti_3C_2T_x$ MXene deposited on Si/SiO$_2$ substrates, while bilayer $Ti_3C_2T_x$ flakes have significantly larger AFM thicknesses of >4 nm.[5,24,25]

Cr_2TiAlC_2 and $Cr_2TiC_2T_x$ were characterized by powder XRD, and the obtained patterns are presented in Fig. 2a. The quality of the parent MAX phase has a significant effect on the MXene synthesis.[6,7,26] The produced Cr_2TiAlC_2 MAX phase was highly crystalline, and no significant impurity phases were recorded. The minor impurities in Cr_2TiAlC_2 were Cr_2AlC and (Ti/Cr)C, which are labeled accordingly in Fig. 2a. The sample for the XRD analysis of $Cr_2TiC_2T_x$ was prepared by vacuum filtering of suspension of MXene flakes and had a layered structure similar to the one shown in Fig. 1e. XRD pattern for the $Cr_2TiC_2T_x$ film shows a major (001) diffraction peak at $2\theta =$

5.9°, which corresponds to the interlayer spacing between the MXene flakes of about 1.5 nm. There are also two smaller peaks at $2\theta = 18.1°$ and 31.2° that represent higher-order (003) and (005) diffractions, respectively, and also originate from the layered structure of the stacked MXene flakes. No diffraction peaks related to the parent MAX phase or other possible crystalline impurities were recorded.

Fig. 2b shows BET data for a dried powder of $Cr_2TiC_2T_x$ flakes. The sample shows a type IV adsorption isotherm with no plateau at high relative pressure (0.8–1), which is observed in mesoporous and macroporous systems. The BET surface area calculated for this sample is 48 m^2 g^{-1}, which is in accordance with reports on other MXene structures.[17]

Finally, we studied $Cr_2TiC_2T_x$ by XPS to investigate the functional groups in the MXene material and its stability during preparation and post-synthesis processing. The results for the freshly prepared $Cr_2TiC_2T_x$ MXene are presented in Fig. 2c–e. The XPS data are consistent with the previous report on
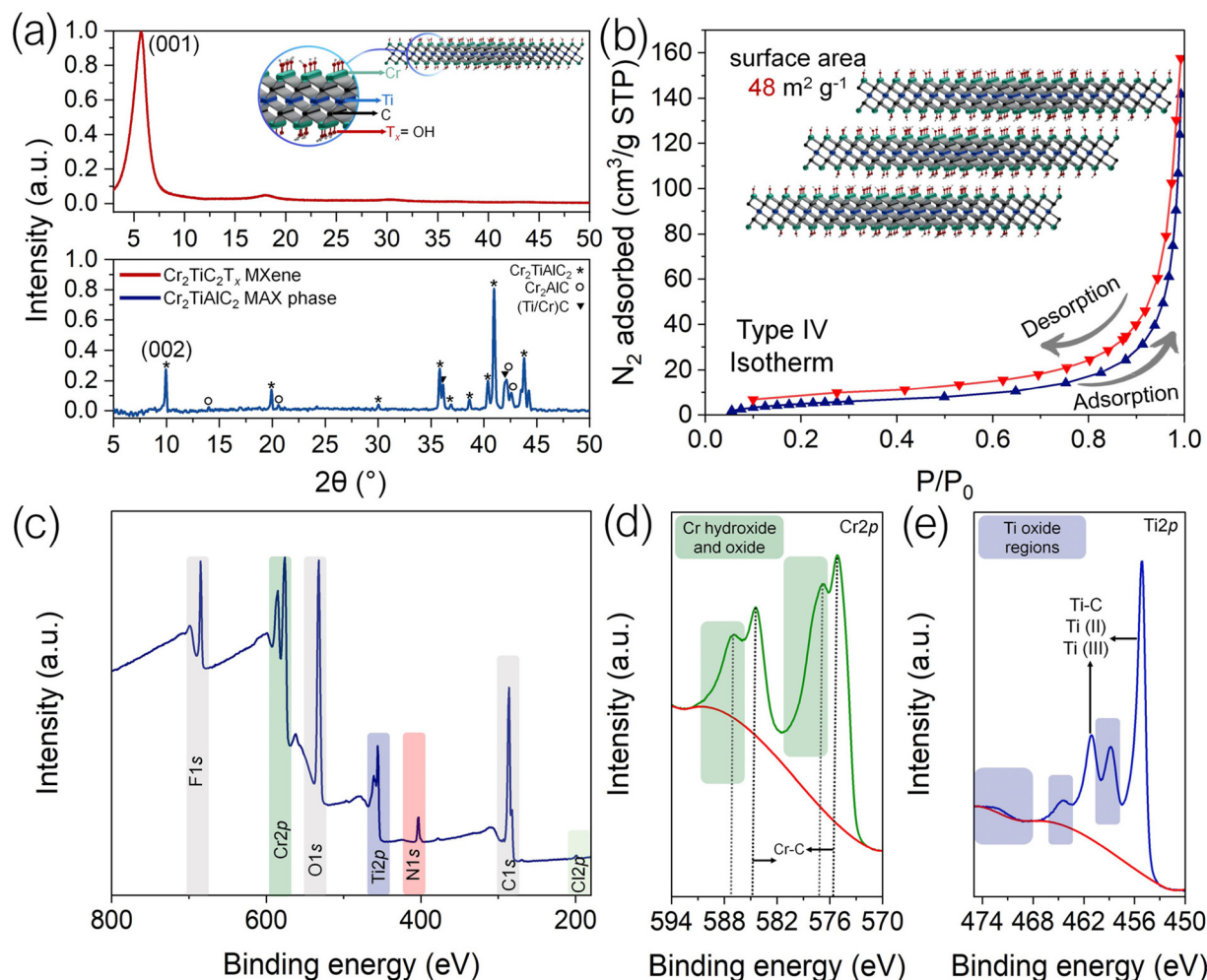

Fig. 2 Materials characterization of $Cr_2TiC_2T_x$ MXene. (a) XRD patterns of the parent Cr_2TiAlC_2 MAX phase (dark blue) and $Cr_2TiC_2T_x$ MXene (red). The peaks related to the MAX phase are labeled with asterisks. The structure of $Cr_2TiC_2T_x$ monolayer is presented in the inset with the terminal groups schematically shown as hydroxyls. (b) BET analysis of a bulk sample of $Cr_2TiC_2T_x$ flakes. (c) XPS survey spectrum of $Cr_2TiC_2T_x$. (d) High-resolution XPS Cr 2p spectrum of $Cr_2TiC_2T_x$. (e) High-resolution XPS Ti 2p spectrum of $Cr_2TiC_2T_x$.

$Cr_2TiC_2T_x$.[9] The major peaks in the XPS survey spectrum in Fig. 2c confirm the presence of Cr, Ti, C, F, and O in $Cr_2TiC_2T_x$, suggesting the –F, –OH, and =O functional groups that are typical for MXenes produced by HF etching.[27] The presence of these functional groups is important for the adsorption of heavy metal cations on the surface of MXene sheets. Fig. S1† shows the deconvoluted spectra of F 1s and O 1s. The XPS F 1s spectrum exhibits a dominant peak at 684.4 eV corresponding to Cr–F and a minor shoulder at 686.6 eV, which we interpret as residual fluoride impurities, such as AlF_3. For O 1s, we assigned the components at 529.7, 531, 532.1, and 533.7 eV to Cr(Ti)–O_x, Cr–O, Cr–OH, and Cr–H_2O, respectively.[9,28] The N 1s peak that is observed in the survey spectrum can be explained by the use of TMAOH as intercalating agent, while the minor Cl 2p peak is present because of the use of HCl for the etching. The high-resolution spectra of

Cr 2p and Ti 2p demonstrate the major metal carbide peaks but also suggest Cr–O and Ti–O bonding. Since we did not observe any visible signs of the MXene degradation in microscopic images, which is typically manifested as oxide particles and pinholes,[25,29] these peaks can be attributed to the presence of oxygen in the C layers of $Cr_2TiC_2T_x$, which was established previously.[8]

3.2. $Cr_2TiC_2T_x$ as a solid phase in d-μ-SPE for trace heavy metal detection

3.2.1. System optimization and adsorption mechanisms.
After the synthesis of $Cr_2TiC_2T_x$, the next step was to study its efficiency for preconcentration of heavy metal ions, Pb^{2+} and Cd^{2+}, for detection by FAAS (see Scheme 1). In the real-life samples analyzed in this study, the concentrations of Pb^{2+} and Cd^{2+} ions were too low for direct detection by FAAS. Therefore,
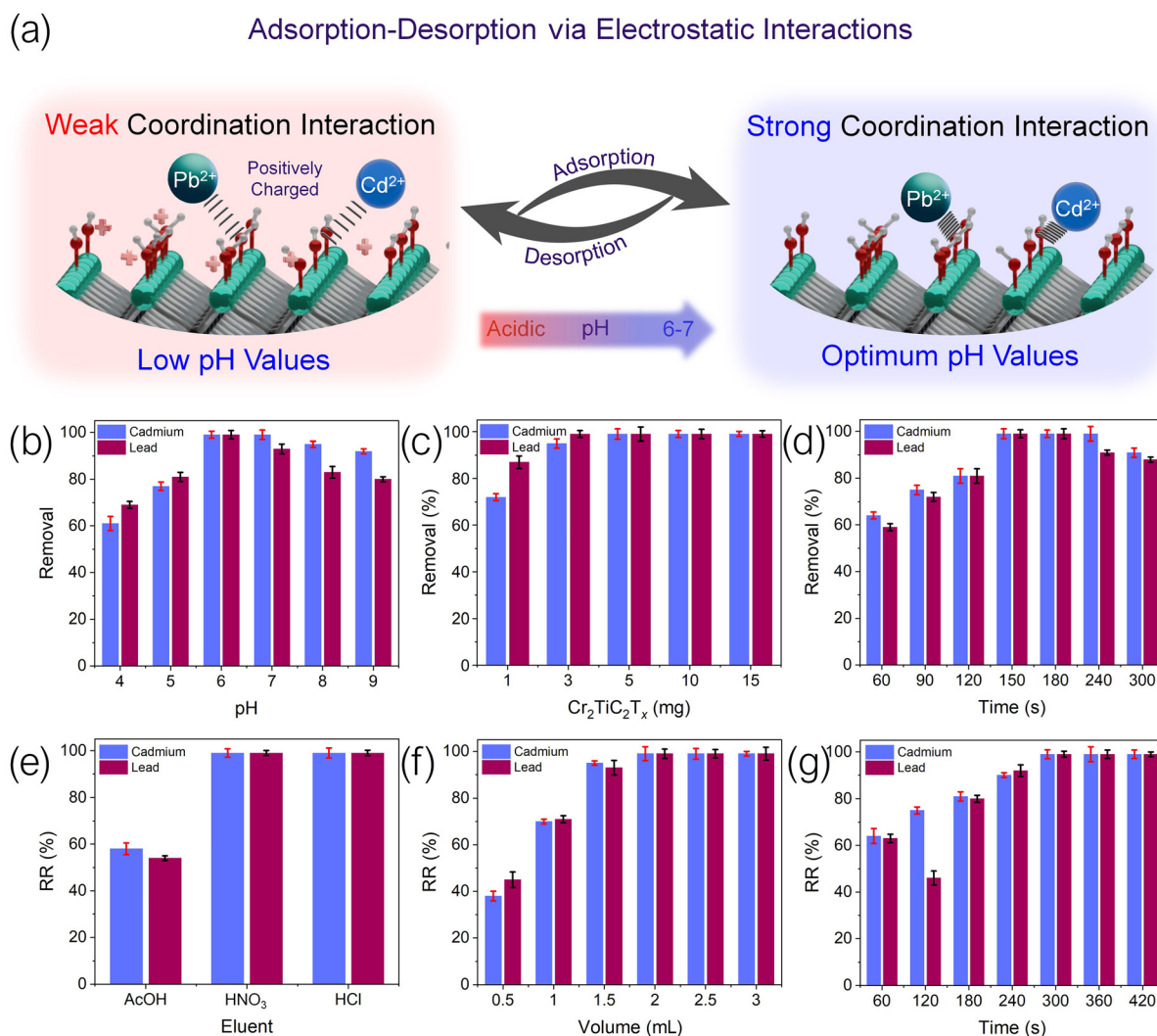

Fig. 3 Adsorption mechanism and system optimization for adsorption and desorption steps. (a) Scheme of the proposed adsorption mechanism based on coordination of heavy metal cations with the surface functional groups of $Cr_2TiC_2T_x$. (b–d) The effect of (b) pH, (c) adsorbent mass, and (d) sonication time on the adsorption of cadmium and lead ions on $Cr_2TiC_2T_x$. (e–g) The effect of (e) eluent type, (f) eluent volume, and (g) sonication time on the desorption of cadmium and lead ions from $Cr_2TiC_2T_x$. The adsorption and desorption steps were optimized using the one-variable-at-a-time approach, keeping the other factors constant.

the role of the MXene material is to adsorb and preconcentrate these ions, enabling their subsequent FAAS analysis (Scheme 1). There are multiple factors affecting the adsorption process in d-μ-SPE, including the pH, the mass of $Cr_2TiC_2T_x$, and the sonication time. We analyzed and optimized these factors using the one-variable-at-a-time method, as summarized in Fig. 3a–d.

The scheme of coordination of heavy metal cations to the surface functional groups of $Cr_2TiC_2T_x$ is shown in Fig. 3a. According to the literature on related adsorbent materials,[30–32] this is likely the main adsorption mechanism, and it is expected to be pH-dependent. For Pb^{2+} and Cd^{2+} ions, the optimal pH was found to be 6 (Fig. 3b). The abundance of protons at low pH values results in positively charged MXene sheets, interfering with the adsorption of cations (Fig. 3a, left panel) and leading to less effective removal of heavy metals. At high pH values, lead and cadmium precipitate as insoluble oxides/hydroxides. The optimal removal of Pb^{2+} and Cd^{2+} was observed at pH 6 (Fig. 3b), when the adsorption of heavy metal cations was most efficient (Fig. 3a, right panel). A recent study suggests a possible presence of chromium vacancies in $Cr_2TiC_2T_x$,[33] which may also provide adsorption sites for Pb^{2+} and Cd^{2+} ions. However, given the likely scarceness of these vacancies compared to the surface functional groups, we still expect the adsorption mechanism shown in Fig. 3a to be dominant in the d-μ-SPE process.

Fig. 3c demonstrates that $Cr_2TiC_2T_x$ exhibits a great adsorption behavior, as evident by its high removal percentage at only 1 mg of adsorbent, especially for Pb^{2+} ions, with removal efficiency reaching 90%. Although complete removal was reached with 3 mg of $Cr_2TiC_2T_x$ adsorbent, we chose 10 mg as the optimized adsorbent mass due to the difficulty in $Cr_2TiC_2T_x$ recovery and the possible loss of material during the desorption steps. The d-μ-SPE method heavily relies on the efficiency of the dispersion of the adsorbent, which in this study was performed by sonication. We reached the highest removal in 150 s, and after 240 s the adsorption–desorption equilibrium shifts toward desorption and reduces the removal efficiency (Fig. 3d). Thus, 150 s was selected as the optimized sonication time for the adsorption step.

The desorption step is affected by the type of eluent, the volume and concentration of the eluent, and the sonication time for the dispersion of the adsorbent. As was the case for the adsorption step, we optimized the abovementioned factors, and the results are summarized in Fig. 3e–g. The most important factor for the desorption is the eluent type. As shown schematically in Fig. 3a, the coordination of heavy metals to the surface groups of $Cr_2TiC_2T_x$ weakens in acidic environment, resulting in desorption of cations from MXene sheets. Fig. 3e demonstrates that for acetic acid as a representative weak acid, the recovery of heavy metal ions was less than 60%. However, strong acids, such as HCl and HNO_3, successfully desorbed Pb^{2+} and Cd^{2+} ions. HCl was selected as the eluent for the next steps as a safer strong acid. The concentration of the acids for the desorption experiments was fixed at 2 M, however, the volume was optimized. Using HCl as the

eluent, volume range of 0.5–3 mL was tested, and 2 mL was sufficient to yield the highest recovery (Fig. 3f). Finally, desorption of heavy metals from the $Cr_2TiC_2T_x$ surface was achieved by sonicating the recovered adsorbent from the adsorption step in 2 mL of HCl (2 M) for 300 s (Fig. 3g). Lower sonication times were not sufficiently effective, leading to lower recovery percentages, while higher sonication times lead to deterioration of the adsorbent during the adsorption–desorption cycles.[30–32]

In summary, based on the results of the system optimization experiments, the optimized conditions for the adsorption of heavy metal ions on MXene sheets include pH 6, an adsorbent mass of 10 mg, and sonication time of 150 s. For the desorption step, the optimized procedure involves the use of 2 mL of 2 M HCl with sonication time of 300 s.

3.2.2. The effect of interfering ions and real-life sample measurements. During selectivity studies, we investigated the interference of prevalent ions in agricultural and food products ($X = Na^+$, K^+, Mg^{2+}, Ca^{2+}, and Zn^{2+}), which introduce up to 5% variation to FAAS analysis.[17] Using a concentration ratio of 250 to 2500 (X/Cd^{2+}, Pb^{2+}), we tested the selectivity of $Cr_2TiC_2T_x$ towards Cd^{2+} and Pb^{2+}. As summarized in Table S1,† no significant interference was observed during adsorption–desorption process under the optimized conditions. Furthermore, we used $Cr_2TiC_2T_x$-based d-μ-SPE method to analyze farm soil and food samples to determine their Cd^{2+} and Pb^{2+} concentrations. After performing the adsorption and desorption steps, the eluent was analyzed with FAAS. The collected data for the real-life samples are summarized

Table 1 Determination of Cd^{2+} and Pb^{2+} ions in real samples

Sample	Element	Added (μg g⁻¹)	Found (μg L⁻¹) ((mean ± ts)/N^{1/2}) $N = 3$, $P_R = 0.05$	RR (%)
Farm soil	Cd	NA[a]	7.96 ± 0.32	—
		25	32.98 ± 0.21	100.10
	Pb	NA	30.53 ± 0.27	—
		25	55.14 ± 0.35	98.44
Shrimp	Cd	NA	8.13 ± 0.33	—
		25	33.11 ± 0.51	99.92
	Pb	NA	ND[b]	—
		25	25.13 ± 0.25	100.52
Cod fish	Cd	NA	6.13 ± 0.21	—
		25	31.27 ± 0.12	100.56
	Pb	NA	ND	—
		25	25.12 ± 0.26	100.48
Coffee beans	Cd	NA	ND	—
		25	25.12 ± 0.12	100.48
	Pb	NA	ND	—
		25	25.09 ± 0.11	100.36
Rice	Cd	NA	5.68	—
		25	30.58 ± 0.12	99.60
	Pb	NA	ND	—
		25	25.18 ± 0.25	100.72

[a] Not added. [b] Not detected.

ized in Table 1. These results demonstrate the practical use of $Cr_2TiC_2T_x$-based d-µ-SPE method for real-life analytical applications.

3.2.3. Method validation, reusability tests, and comparison studies.

The limits of detection (LODs) for Pb^{2+} and Cd^{2+} were extracted from the analytical calibration curves for both heavy metal ions. As shown in Fig. S2,† the calibration curves, plotted for these ions under the optimized conditions, show LODs of 0.09 and 1.9 ng mL^{-1} with linear dynamic ranges of 0.3–90 µg L^{-1} and 6–120 µg L^{-1} for Cd^{2+} and Pb^{2+}, respectively. Also, the extraction efficiency was found to be greater than 97%, with a relative standard deviation (RSD) of less than 3%. The calculated R^2 values for Cd^{2+} and Pb^{2+} ions were 0.999 and 0.996, respectively. Additionally, Taiwan Clay Soil (CRM046)-certified reference material with a standard amount of cadmium and lead ions was used to validate the $Cr_2TiC_2T_x$-based d-µ-SPE method. At the optimized conditions (Fig. 3),

the relative errors for Cd^{2+} and Pb^{2+} ions were −0.42 and −0.95% (Table S2†), respectively, showing that the proposed $Cr_2TiC_2T_x$-based d-µ-SPE method has great potential as a reliable and accurate method for the detection of Cd^{2+} and Pb^{2+} ions in real-life samples.

The stability of the MXene adsorbent over several cycles of adsorption and desorption was tested and an acceptable performance of about 96% of the initial performance was recorded for up to six cycles. By the tenth cycle, the performance decreased to 91% (Fig. 4a), likely due to sonication and loss of adsorbent. After the sixth cycle, XPS and electron microscopy were performed on the recovered $Cr_2TiC_2T_x$ samples (Fig. 4b–g). The XPS Ti 2p and Cr 2p spectra of the MXene recovered after six cycles look very similar to the spectra of the freshly prepared $Cr_2TiC_2T_x$ (Fig. 4b and c). While there is a noticeable increase of the XPS signal in the oxide regions of the spectra after six d-µ-SPE cycles, the change is rather small compared to oxidized
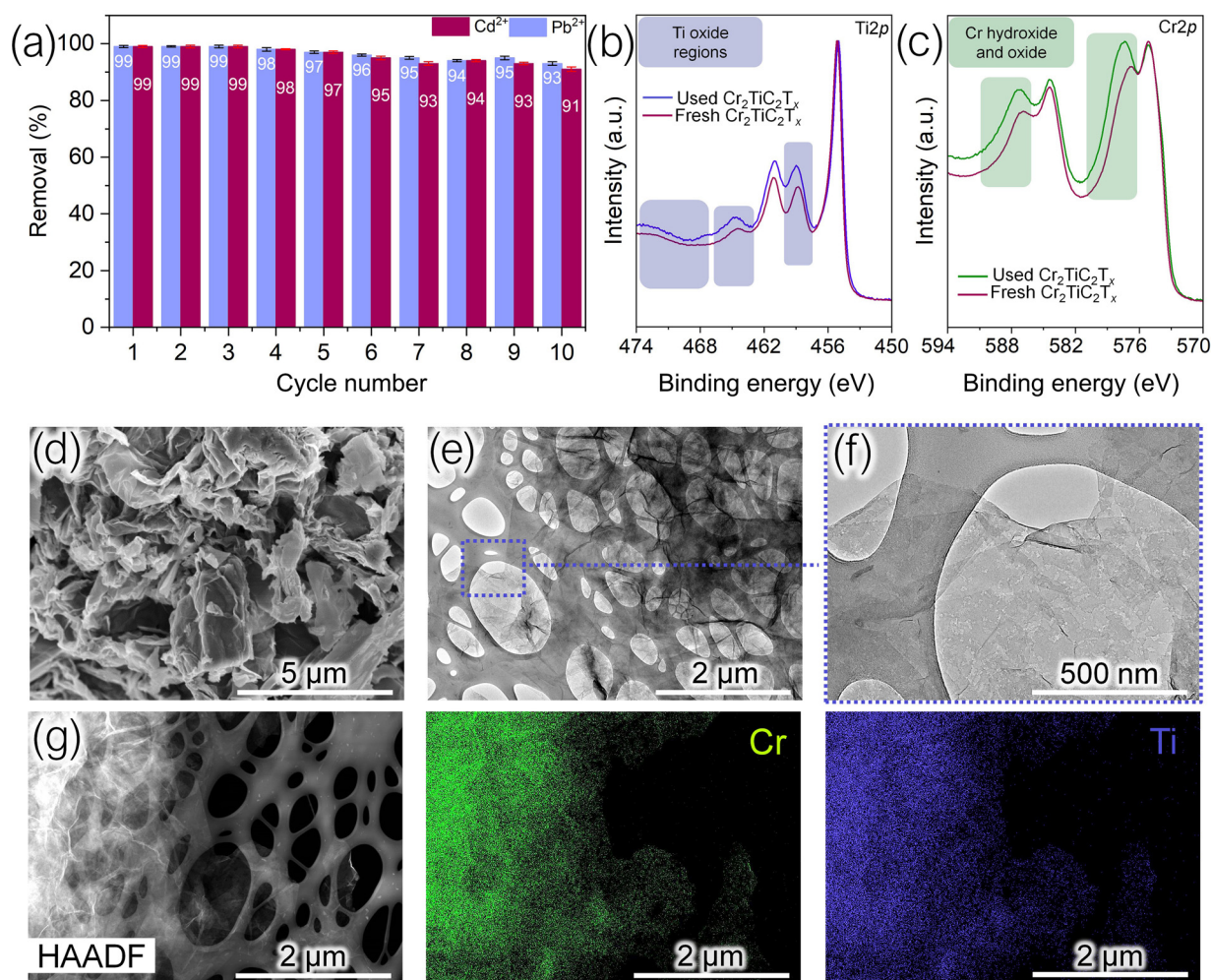

Fig. 4 Reusability study and materials characterization of recovered $Cr_2TiC_2T_x$ adsorbent. (a) Removal efficiency of reused $Cr_2TiC_2T_x$ in ten cycles of adsorption and desorption of Pb^{2+} and Cd^{2+} ions. (b) Comparison of high-resolution XPS Ti 2p spectra of the as-prepared $Cr_2TiC_2T_x$ and the sample recovered after six d-µ-SPE cycles. (c) Comparison of high-resolution XPS Cr 2p spectra of the as-prepared $Cr_2TiC_2T_x$ and the sample recovered after six d-µ-SPE cycles. (d) SEM image of $Cr_2TiC_2T_x$ flakes after six d-µ-SPE cycles. (e and f) TEM images of the same flakes dispersed on a lacey carbon grid. (g) STEM image of the same sample and elemental EDX maps for Cr and Ti.

Table 2 Comparison of the presented method with previously published reports

Material	Method	LOD (Cd^{2+}) (ng mL^{-1})	LOD (Pb^{2+}) (ng mL^{-1})	Ref.
MOF-derived BCN	Electrochemical	0.41	0.93	35
MWCNT-2Fe$_3$O$_4$@SiO$_2$-SH	VA-DMSPE-GFAAS	0.09	—	36
Ag modified ZnO	d-μ-SPE-FAAS	—	32.7	37
B. subtilis-MWCNT	SPE-ICP-OES	—	0.024	38
KCC-1	d-μ-SPE-GFAAS	0.02	0.18	39
Magnetic orange peel powder	DMSS-FAAS	—	2.64	40
NH$_2$/SH-functionalized Ti$_3$C$_2$T$_x$	d-μ-SPE-FAAS	0.12	2.30	17
Cr$_2$TiC$_2$T$_x$	d-μ-SPE-FAAS	0.09	1.9	This work

MXene samples reported in literature,[25,29] where the metal oxide peaks become much more intense than the metal carbide peaks. Therefore, the XPS results suggest modest degradation of Cr$_2$TiC$_2$T$_x$ after six d-μ-SPE cycles.

SEM image of Cr$_2$TiC$_2$T$_x$ that was recovered after six d-μ-SPE cycles (Fig. 4d) shows that the material retains its sheet-like morphology. Although the flakes appear aggregated and crumpled, this appearance is typical for dried MXene samples. A closer inspection of these flakes by TEM (Fig. 4e and f) demonstrates mesoscopic holes and tears, suggesting some degradation of Cr$_2$TiC$_2$T$_x$ during the cycles, although we did not observe oxide particles decorating the flake edges, which typically appear when the oxidation of MXene sheets becomes more extensive.[25,29,34] Some tearing of Cr$_2$TiC$_2$T$_x$ flakes could be caused by sonication[5,7] that was extensively used in the d-μ-SPE cycles. The STEM-EDX analysis (Fig. 4g) of the recovered MXene sample shows uniform elemental distribution of Cr and Ti, similar to the freshly prepared Cr$_2$TiC$_2$T$_x$. Overall, these results suggest modest degradation of Cr$_2$TiC$_2$T$_x$ from cycle to cycle, so that the adsorbent material can be reused multiple times for efficient d-μ-SPE.

Finally, the developed Cr$_2$TiC$_2$T$_x$-based d-μ-SPE was compared with other methods and materials from recent literature, as summarized in Table 2. The Cr$_2$TiC$_2$T$_x$-based d-μ-SPE method shows a high performance and often exceeds the LOD values reported for other functionalized nanomaterials.

4. Conclusions

This work demonstrates that Cr$_2$TiC$_2$T$_x$ MXene is an efficient adsorbent for the d-μ-SPE method for trace detection of heavy metals in real-life samples. We synthesized a high-quality Cr$_2$TiC$_2$T$_x$ and demonstrated uniform monolayer flakes with sizes in the μm range. The bulk MXene material had a BET surface area of 48 m^2 g^{-1}. We tested Cr$_2$TiC$_2$T$_x$ for the adsorption and desorption of Pb^{2+} and Cd^{2+} ions and determined the following optimized conditions: for the adsorption step, pH 6, 10 mg of Cr$_2$TiC$_2$T$_x$ as adsorbent, and sonication time of 150 s, and for the desorption step, 2 mL of 2 M HCl and sonication time of 300 s. Cr$_2$TiC$_2$T$_x$ was shown as an efficient tool for preconcentrating heavy metal ions from agricultural samples followed by FAAS analysis. The developed method, Cr$_2$TiC$_2$T$_x$-d-μ-SPE, holds a great promise with attractive figures of merits. The LOD values for Cd^{2+} and Pb^{2+} ions were 0.09 and 1.9 ng

mL^{-1}, with large linear dynamic ranges of 0.3–90 and 6–110 ng mL^{-1}, respectively. After the use, the MXene can be recovered for another d-μ-SPE, and in six consecutive cycles the material showed a performance of at least 96% of the first analytical experiment. By the tenth cycle, the performance decreased to 91%, likely due to sonication and loss of adsorbent. The results of experiments with interfering ions showed a promising Cr$_2$TiC$_2$T$_x$-d-μ-SPE performance with relative recoveries in a range of 99.67–102.34% and 99.78–101.18% for lead and cadmium ions, respectively.

This study shows that Cr$_2$TiC$_2$T$_x$ is highly efficient, selective, and reliable adsorbent that can open new avenues for addressing environmental and food safety challenges. Future studies of Cr$_2$TiC$_2$T$_x$ could explore the possibility of its surface functionalization to improve the performance of the material as an adsorbent and tailor it for specific analytical applications. Furthermore, while most studies in the field of MXenes focus on Ti$_3$C$_2$T$_x$, this work demonstrates that there is a great promise in exploring other MXene materials as well. For example, we demonstrate that as an adsorbent for the d-μ-SPE method, Cr$_2$TiC$_2$T$_x$ had better LOD values than NH$_2$/SH-functionalized Ti$_3$C$_2$T$_x$ that we tested in our previous study (Table 2).[17] This result warrants an investigation of other MXene materials beyond Ti$_3$C$_2$T$_x$ for analytical applications.

Data availability

The data supporting this article have been included as part of the ESI.†

Conflicts of interest

The authors declare no conflict of interest.

Acknowledgements

References

1 Y. Gogotsi and B. Anasori, *ACS Nano*, 2019, **13**, 8491–8494.

2 B. Anasori and Y. Gogotsi, *2D Metal Carbides and Nitrides (MXenes): Structure, Properties and Applications*, Springer International Publishing, 2019.

3 A. Vahidmohammadi, J. Rosen and Y. Gogotsi, *Science*, 2021, **372**, eabf1581.

4 M. Naguib, M. Kurtoglu, V. Presser, J. Lu, J. Niu, M. Heon, L. Hultman, Y. Gogotsi and M. W. Barsoum, *Adv. Mater.*, 2011, **23**, 4248–4253.

5 A. Lipatov, M. Alhabeb, M. R. Lukatskaya, A. Boson, Y. Gogotsi and A. Sinitskii, *Adv. Electron. Mater.*, 2016, **2**, 1600255.

6 T. S. Mathis, K. Maleski, A. Goad, A. Sarycheva, M. Anayee, A. C. Foucher, K. Hantanasirisakul, C. E. Shuck, E. A. Stach and Y. Gogotsi, *ACS Nano*, 2021, **15**, 6420–6429.

7 M. Shekhirev, J. Busa, C. E. Shuck, A. Torres, S. Bagheri, A. Sinitskii and Y. Gogotsi, *ACS Nano*, 2022, **16**, 13695–13703.

8 P. P. Michałowski, M. Anayee, T. S. Mathis, S. Kozdra, A. Wójcik, K. Hantanasirisakul, I. Jóźwik, A. Piątkowska, M. Możdżonek, A. Malinowska, R. Diduszko, E. Wierzbicka and Y. Gogotsi, *Nat. Nanotechnol.*, 2022, **17**, 1192–1197.

9 K. Hantanasirisakul, B. Anasori, S. Nemsak, J. L. Hart, J. Wu, Y. Yang, R. V. Chopdekar, P. Shafer, A. F. May, E. J. Moon, J. Zhou, Q. Zhang, M. L. Taheri, S. J. May and Y. Gogotsi, *Nanoscale Horiz.*, 2020, **5**, 1557–1565.

10 D. Mohanadas, R. Rohani, Y. Sulaiman, S. A. Bakar, E. Mahmoudi and L.-C. Zhang, *Mater. Today Sustainability*, 2023, **22**, 100411.

11 Y. Sheth, S. Dharaskar, V. Chaudhary, M. Khalid and R. Walvekar, *Chemosphere*, 2022, **293**, 133563.

12 Z. Othman, H. R. Mackey and K. A. Mahmoud, *Chemosphere*, 2022, **295**, 133849.

13 M. Bilal and I. Ihsanullah, *J. Water Process Eng.*, 2022, **49**, 103010.

14 M. Kandeel, A. Turki Jalil, M. Hadi Lafta, S. Ziyadullaev and Y. Fakri Mustafa, *Microchem. J.*, 2022, **183**, 108121.

15 A. Dhillon, N. Singh, M. Nair and D. Kumar, *Chemosphere*, 2022, **303**, 135166.

16 A. S. Jatoi, N. M. Mubarak, Z. Hashmi, N. H. Solangi, R. R. Karri, Y. H. Tan, S. A. Mazari, J. R. Koduru and A. Alfantazi, *Chemosphere*, 2023, **313**, 137497.

17 S. Bagheri, R. Chilcott, S. Luo and A. Sinitskii, *Langmuir*, 2022, **38**, 12924–12934.

18 A. Parihar, N. K. Choudhary, P. Sharma and R. Khan, *Environ. Pollut.*, 2023, **316**, 120695.

19 X. Zhang, D. An, Z. Bi, W. Shan, B. Zhu, L. Zhou, L. Yu, H. Zhang, S. Xia and M. Qiu, *J. Electroanal. Chem.*, 2022, **911**, 116239.

20 K. Rizwan, A. Rahdar, M. Bilal and H. M. N. Iqbal, *Chemosphere*, 2022, **291**, 132820.

21 S. Hao, C. Liu, X. Chen, B. Zong, X. Wei, Q. Li, H. Qin and S. Mao, *J. Hazard. Mater.*, 2021, **418**, 126301.

22 X. Zhu, B. Liu, H. Hou, Z. Huang, K. M. Zeinu, L. Huang, X. Yuan, D. Guo, J. Hu and J. Yang, *Electrochim. Acta*, 2017, **248**, 46–57.

23 S. Bagheri, A. Lipatov, N. S. Vorobeva and A. Sinitskii, *ACS Nano*, 2023, **17**, 18747–18757.

24 A. Lipatov, H. Lu, M. Alhabeb, B. Anasori, A. Gruverman, Y. Gogotsi and A. Sinitskii, *Sci. Adv.*, 2018, **4**, eaat0491.

25 H. Pazniak, I. A. Plugin, M. J. Loes, T. M. Inerbaev, I. N. Burmistrov, M. Gorshenkov, J. Polcak, A. S. Varezhnikov, M. Sommer, D. V. Kuznetsov, M. Bruns, F. S. Fedorov, N. S. Vorobeva, A. Sinitskii and V. V. Sysoev, *ACS Appl. Nano Mater.*, 2020, **3**, 3195–3204.

26 C. E. Shuck, M. Han, K. Maleski, K. Hantanasirisakul, S. J. Kim, J. Choi, W. E. B. Reil and Y. Gogotsi, *ACS Appl. Nano Mater.*, 2019, **2**, 3368–3376.

27 J. Halim, K. M. Cook, M. Naguib, P. Eklund, Y. Gogotsi, J. Rosen and M. W. Barsoum, *Appl. Surf. Sci.*, 2016, **362**, 406–417.

28 P. A. Maughan, L. Bouscarrat, V. R. Seymour, S. Shao, S. J. Haigh, R. Dawson, N. Tapia-Ruiz and N. Bimbo, *Nanoscale Adv.*, 2021, **3**, 3145–3158.

29 M. J. Loes, S. Bagheri, N. S. Vorobeva, J. Abourahma and A. Sinitskii, *ACS Appl. Nano Mater.*, 2023, **6**, 9226–9235.

30 Y. Zhang, L. Wang, N. Zhang and Z. Zhou, *RSC Adv.*, 2018, **8**, 19895–19905.

31 B. M. Jun, S. Kim, J. Heo, C. M. Park, N. Her, M. Jang, Y. Huang, J. Han and Y. Yoon, *Nano Res.*, 2018, **12**, 471–487.

32 K. Rasool, R. P. Pandey, P. A. Rasheed, S. Buczek, Y. Gogotsi and K. A. Mahmoud, *Mater. Today*, 2019, **30**, 80–102.

33 S. Bagheri, M. J. Loes, A. Lipatov, K. Acharya, T. R. Paudel, H. Lu, R. Khurana, M. I. Kholil, A. Gruverman and A. Sinitskii, *Matter*, 2024, **7**, 4281–4296.

34 A. Sarycheva, M. Shanmugasundaram, A. Krayev and Y. Gogotsi, *ACS Nano*, 2022, **16**, 6858–6865.

35 R. Huang, J. Lv, J. Chen, Y. Zhu, J. Zhu, T. Wågberg and G. Hu, *J. Hazard. Mater.*, 2023, **442**, 130020.

36 P. d. S. Morales, P. M. dos Santos, A. E. De Carvalho and M. Z. Corazza, *Food Chem.*, 2022, **368**, 130823.

37 O. Ozalp and M. Soylak, *Talanta*, 2023, **253**, 124082.

38 S. Ozdemir, A. Dündar, N. Dizge, E. Kılınç, D. Balakrishnan, K. S. Prasad and N. Senthilkuma, *Chemosphere*, 2023, **317**, 137840.

39 M. Behbahani, G. Rabiee, S. Bagheri and M. M. Amini, *Microchem. J.*, 2022, **183**, 107951.

40 F. A. Borges, L. M. Costa, C. e. R. T. Tarley, G. d. F. a. L. Martins and E. C. Figueiredo, *Food Chem.*, 2023, **413**, 135676.